

## Article

# Effects of Recrystallization on Tensile Anisotropic Properties for IN738LC Fabricated by Laser Powder Bed Fusion

Shinya Hibino <sup>1,2,\*</sup> , Kazushige Fujimitsu <sup>2</sup>, Makoto Azuma <sup>2</sup>, Takuya Ishimoto <sup>1,3</sup>  and Takayoshi Nakano <sup>1,3,\*</sup> 

<sup>1</sup> Division of Materials and Manufacturing Science, Graduate School of Engineering, Osaka University, 2-1, Yamadaoka, Suita 565-0871, Japan; ishimoto@mat.eng.osaka-u.ac.jp

<sup>2</sup> Technical Institute, Kawasaki Heavy Industries, Ltd., 1-1, Kawasaki-cho, Akashi 673-8666, Japan; fujimitsu\_kazushige@khi.co.jp (K.F.); azuma\_m@khi.co.jp (M.A.)

<sup>3</sup> Anisotropic Design & Additive Manufacturing Research Center, Osaka University, 2-1, Yamadaoka, Suita 565-0871, Japan

\* Correspondence: hibino\_shinya@khi.co.jp (S.H.); nakano@mat.eng.osaka-u.ac.jp (T.N.)

**Abstract:** This study demonstrates the effects of recrystallization on tensile properties and the anisotropy of IN738LC, a typical  $\gamma'$  precipitation-strengthened alloy, at both room and high temperatures via the laser powder bed fusion process. The nonrecrystallized columnar microstructure, subjected to standard IN738LC heat treatment up to 1120 °C, and the almost fully recrystallized microstructure, heat-treated at 1204 °C, were compared. The tensile properties strongly depend on whether recrystallization was completed as well as the tensile direction. This can be explained by microstructure characterization, featuring the Taylor factor in the tensile direction, average grain size estimated by ellipse approximation, and the relationship between the grain shape and tensile direction. The shape of the recrystallized grains and the distribution of coarse MC carbides inside the recrystallized grains were determined by the microstructure in an as-built state. In high-temperature tensile tests conducted in the horizontal direction, the separation of the columnar grains caused a brittle fracture. In contrast, dimples were observed at the fracture surface after recrystallization, indicating scope for further improvement in ductility.

**Keywords:** laser powder bed fusion; IN738LC; heat treatment; recrystallization; MC carbide; anisotropy; tensile property



**Citation:** Hibino, S.; Fujimitsu, K.; Azuma, M.; Ishimoto, T.; Nakano, T. Effects of Recrystallization on Tensile Anisotropic Properties for IN738LC Fabricated by Laser Powder Bed Fusion. *Crystals* **2022**, *12*, 842. <https://doi.org/10.3390/cryst12060842>

Academic Editor: Umberto Prisco

Received: 26 May 2022

Accepted: 13 June 2022

Published: 15 June 2022

**Publisher's Note:** MDPI stays neutral with regard to jurisdictional claims in published maps and institutional affiliations.



**Copyright:** © 2022 by the authors. Licensee MDPI, Basel, Switzerland. This article is an open access article distributed under the terms and conditions of the Creative Commons Attribution (CC BY) license (<https://creativecommons.org/licenses/by/4.0/>).

## 1. Introduction

Additive manufacturing (AM) is a highly promising method that enables the production of arbitrary three-dimensional shapes [1–3]. Many studies have been conducted on a wide variety of materials, such as stainless steels [4–6], aluminum alloys [7], titanium alloys [8,9], high-entropy alloys [10,11], and intermetallic compounds [12], for various industrial applications. For Ni-based superalloys, the major applications are considered to be gas turbine parts [13]. The laser powder bed fusion (LPBF) process, a typical metal AM process, enables the precision manufacturing of fine complex structures and hollow channels [2,14,15]. Since Ni-based superalloys have difficulty in machining, welding, and forming, limited part shapes can be manufactured. The LPBF process is expected to overcome these limitations, and certain demonstrations, including combustor burners and turbine blades, have been reported to date [16,17].

The LPBF process is metallurgically characterized by fast cooling rates and large temperature gradients [18]. Anisotropic microstructures evolve based on cell solidification along the cooling direction within a melt pool [19,20]. The adoption of appropriate process parameters (laser power, scanning speed, hatch distance, layer thickness, scanning strategy, etc.) results in a variety of distinct microstructures, including single crystalline-like microstructures, crystallographic lamellar microstructures, and polycrystalline microstructures [21–24]. These microstructures, uniquely obtained by the LPBF process, provide

excellent oxidation resistance [25], enhance corrosion resistance [5,22], and enable control of the mechanical properties [23,26,27].

Generally, Ni-based superalloys can be classified into three types of strengthening mechanisms: solid solution-strengthened alloys (typically Hastelloy-X [28]),  $\gamma''$  ( $\text{Ni}_3\text{Nb}$  phase) precipitation-strengthened alloys (typically IN718 [29]), and  $\gamma'$  ( $\text{Ni}_3(\text{Al}, \text{Ti})$  phase) precipitation-strengthened alloys (IN939 [30], IN738LC [31], IN713LC [32], and CM247LC [33]). Among these superalloys, the  $\gamma'$  precipitation-strengthened alloys with the highest strength at high temperatures were created by a combination of complex techniques such as precipitate design, anisotropic crystallographic orientation control, and grain boundary strengthening [34]. To obtain the designed microstructure and mechanical properties, the chemical composition and heat treatment conditions were defined, considering that the alloys are castings. Therefore, for LPBF-processed  $\gamma'$  precipitation-strengthened alloys, it is necessary to redesign the standard manufacturing route and evaluate the mechanical properties exhibited by the microstructure.

Several studies on the heat treatment of LPBF-processed  $\gamma'$  precipitation-strengthened alloys have been performed. Kunze et al. [35] reported that heat treatment at 1180 °C did not cause recrystallization and that the microstructure evolved via the LPBF process remained, whereas Muñoz-Moreno et al. [33] reported that heat treatment at 1230 °C caused full recrystallization, resulting in isotropic Young's modulus. Further studies on the recrystallization process, such as the effect of carbide formation on recrystallization [36], are required. Kanagarajah et al. [30] and Zhao et al. [32] examined the anisotropy of tensile properties between the vertical (building direction) and horizontal directions. Although low ductility was observed in horizontal tests, a detailed discussion on the relationship between the anisotropy of the tensile properties, low ductility, microstructure evolution via the LPBF process, and recrystallization during heat treatment has not been performed.

Therefore, further investigation of recrystallization and its effect on mechanical properties is required for LPBF-processed  $\gamma'$  precipitation-strengthened alloys. In particular, this study focuses on the effect of recrystallization on the tensile properties at room and high temperatures through a detailed analysis of the microstructure characterized by the Taylor factor, average grain size, and grain shape before and after recrystallization. In addition, this study clarifies the factors that cause anisotropic tensile properties, including low ductility in the horizontal direction. This study will lead to the elucidation of how the mechanical properties of LPBF-processed  $\gamma'$  precipitation-strengthened alloys are determined and contribute to the determination of industrial manufacturing processes utilizing the LPBF process, such as optimal heat treatment conditions.

## 2. Materials and Methods

### 2.1. Fabrication of IN738LC Samples via LPBF Process

Gas-atomized IN738LC powder (Oerlikon, Westbury, NY, USA) with the chemical composition listed in Table 1 was used in this study. Scanning electron microscopy (scanning electron microscope; SEM, SU5000, Hitachi High-Tech, Tokyo, Japan) images of IN738LC powder are shown in Figure 1a. The particle size distribution curves measured by the laser scattering diffraction-type particle size distribution meter (MT3300EX II, Microtrac, Montgomeryville, PA, USA) are as shown in Figure 1b, where  $D_{10}$  is 21.4  $\mu\text{m}$ ,  $D_{50}$  is 33.0  $\mu\text{m}$ , and  $D_{90}$  is 50.8  $\mu\text{m}$ .

The LPBF process was followed using LPBF equipment (EOS M290, EOS, Krailing, Germany) equipped with a Yb fiber laser with a maximum output of 400 W. To avoid unintentional temperature changes owing to the laser energy input, the base plate was preheated to 80 °C. The oxygen concentration was maintained below 100 ppm by filling the building chamber with high-purity Ar gas. Vertical samples (Figure 1c, called "Z-sample(s)") of 8 mm diameter and 60 mm height (z-direction) and horizontal samples (Figure 1d, called "X-sample(s)") with dimensions 60 mm (x-direction), 8 mm (y-direction), and 8 mm (z-direction) were built directly on the base plate and then cut off in the vicinity of the plate. To determine the effect of the microstructure itself on mechanical properties,

the volumetric energy density  $E_{vol}$  [ $J/mm^3$ ] was set to  $72.9 J/mm^3$  [37], which has been reported to produce dense products without lack-of-fusion and keyhole-type defects [26]. To handle the  $x$ – $y$  plane isotropically, the rotation scanning strategy [38] was employed, in which bidirectional laser scanning was rotated by  $67^\circ$  layer by layer. However, to avoid laser scanning parallel to the Ar gas flow direction ( $-y$ -direction), when the scanning direction was within a range of  $\pm 30^\circ$  from the  $y$ -direction, the rotation angle was skipped and additionally rotated by  $67^\circ$ . The exposure area in each layer was divided into stripes of a width of 10 mm, and each stripe was exposed in order [38]. A schematic of these complex laser scanning behaviors is shown in Figure 2.

**Table 1.** Chemical composition of IN738LC powder.

Element	Ni	Co	Cr	Mo	W	Nb	Ta	Al	Ti	Fe	C	B	Zr
Composition (wt.%)	Bal.	8.6	16.2	1.8	2.7	0.9	1.8	3.4	3.5	3.8	0.13	0.004	0.07

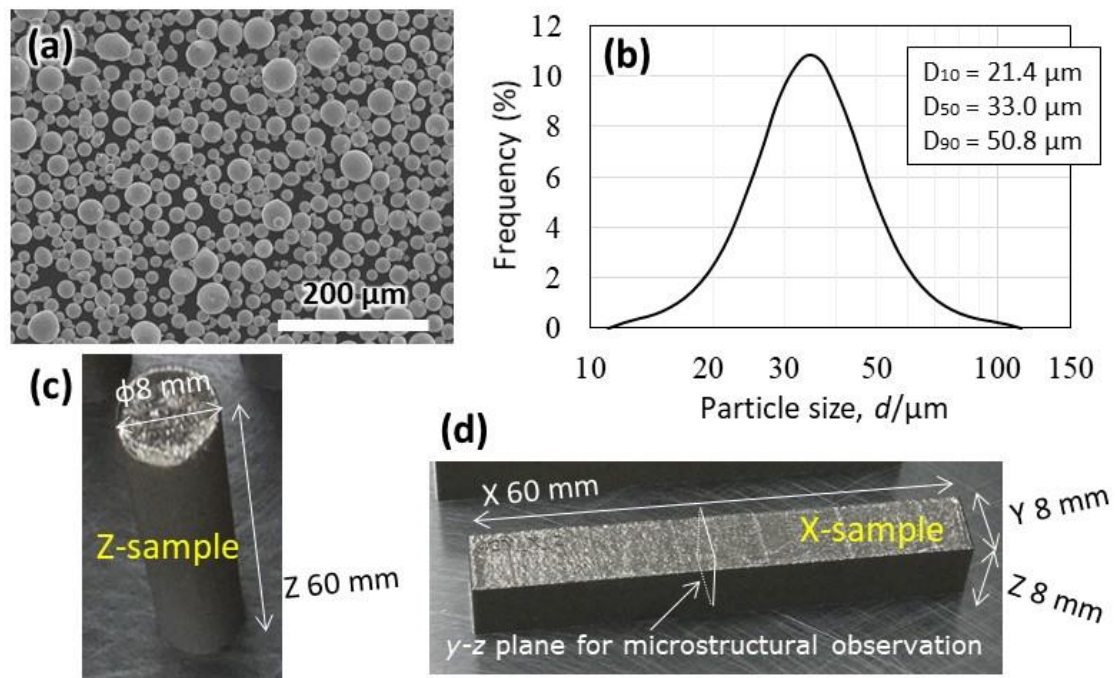


**Figure 1.** (a) SEM image and (b) particle size distribution of IN738LC powder, and pictures of (c) Z-sample and (d) X-sample along the  $z$ -direction and the  $x$ -direction, respectively.

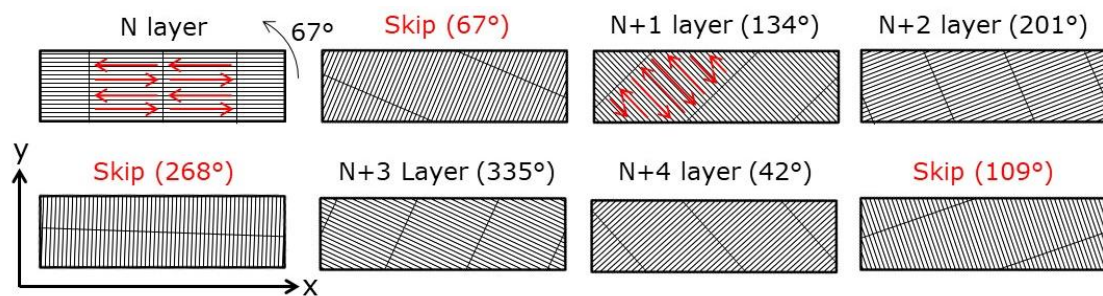


**Figure 2.** Schematic of  $67^\circ$  rotating scanning strategy with 10 mm width stripes.

## 2.2. Heat Treatments

IN738LC built samples were subjected to two heat treatment conditions. The first is the standard condition for IN738LC casting [39]. The solution treatment (ST) was performed

at 1120 °C for 2 h followed by Ar gas fan cooling, and then aging was subjected to 843 °C for 24 h. Hereafter, this first condition will be referred to as “L-HT.” The second condition consisted of stress relief (SR), hot isostatic pressing treatment (HIP), ST, and aging to promote recrystallization. The SR condition was arbitrary as long as the SR temperature was lower than the latter heat treatment temperature. The HIP treatment was performed at 1204 °C for 4 h in a 104 MPa Ar atmosphere. The ST was subjected to 1204 °C for 2 h, followed by Ar gas fan cooling. The aging process was the same as that for L-HT. This second condition is hereafter referred to as “H-HT.” The as-built state without heat treatment is called “AB.” A summary of the heat treatment conditions is presented in Table 2.

**Table 2.** Heat treatment conditions for IN738LC built samples.

Abbreviation	Stress Relief (SR)	Hot Isostatic Pressing (HIP)	Solution Treatment (ST)	Aging
AB	-	-	-	-
L-HT	-	-	1120 °C 2 h	843 °C 24 h
H-HT	Below 1204 °C Up to 2 h	1204 °C 4 h	1204 °C 2 h	843 °C 24 h

### 2.3. Microstructure Characterization

As the initial preparation for microstructure observation, the X-sample was cut on the *y-z* plane, embedded in resin, and polished with emery paper and then with colloidal silica. The observation positions were all near the center of the built samples. An electron backscatter diffraction (EBSD) detector, Pegasus Digiview 5 (EDAX, Pleasanton, CA, USA) was equipped in the SEM and used. The magnification was 100×, the acceleration voltage was 15 kV, and the step size was 2 μm. Pole figures, inverse pole figure (IPF) maps, kernel average misorientation (KAM) maps, Taylor factor, and average grain size (using elliptical approximation) were obtained using OIM Data Collection and OIM Analysis ver. 8 (EDAX, Pleasanton, CA, USA). The composition of the precipitates was determined using energy dispersive X-ray spectroscopy (EDX; Pegasus Octane Elect Plus, EDAX, Pleasanton, CA, USA).

### 2.4. Tensile Tests

The X- and Z-samples, which had been subjected to aging treatment, were cut into tensile specimens of 4 mm diameter and 20 mm gauge length. Instron 5982 (Instron, Norwood, MA, USA) was used for the tensile tests at room temperatures of 23 °C (according to ASTM E8M) and 760 °C (according to ASTM E21). The test atmosphere was atmospheric, and three tests were conducted for each condition. After the tensile tests, the fracture surfaces were observed using the EDX-SEM system.

## 3. Results

### 3.1. Microstructure Characterization before and after Heat Treatments

Due to the LPBF fabrication at optimum energy density, no obvious defects were present, and the raw powder was completely melted and fused. The IPF maps, KAM maps, and {001} pole figures are shown in Figure 3. Microstructural evolution via heat treatment was observed. The AB- and L-HT-ed materials had columnar grains along the *z*-direction, with no change in grain shape observed after L-HT. The columnar grains exhibited the first orientation in the [001]//*z*-direction, and the second orientation was rotated randomly in the *x*-direction. This is considered to be a result of the rotation scan strategy, which is consistent with the report by Sun et al. [21] representing that the columnar grains evolved by the rotation scan strategy. In the {001} pole figure of the AB material (Figure 3g), the orientation in the *y*-direction// [010] was weak. This weakness was considered a result of the skip of the laser scanning parallel to the *y*-direction. As indicated by the KAM map, the AB- and L-HT-ed materials exhibited high residual strain. In contrast, H-HT resulted

in a recrystallized microstructure, as shown in Figure 3c. Most recrystallized grains had elliptical or rectangular shapes along the z-direction. Although there was little residual strain in the H-HT-ed material, recrystallization did not occur in a few grains, as shown in Figure 3j. The  $\{001\}$  pole figure after recrystallization (Figure 3i) shows a weak  $[001]$  orientation in the z-direction.

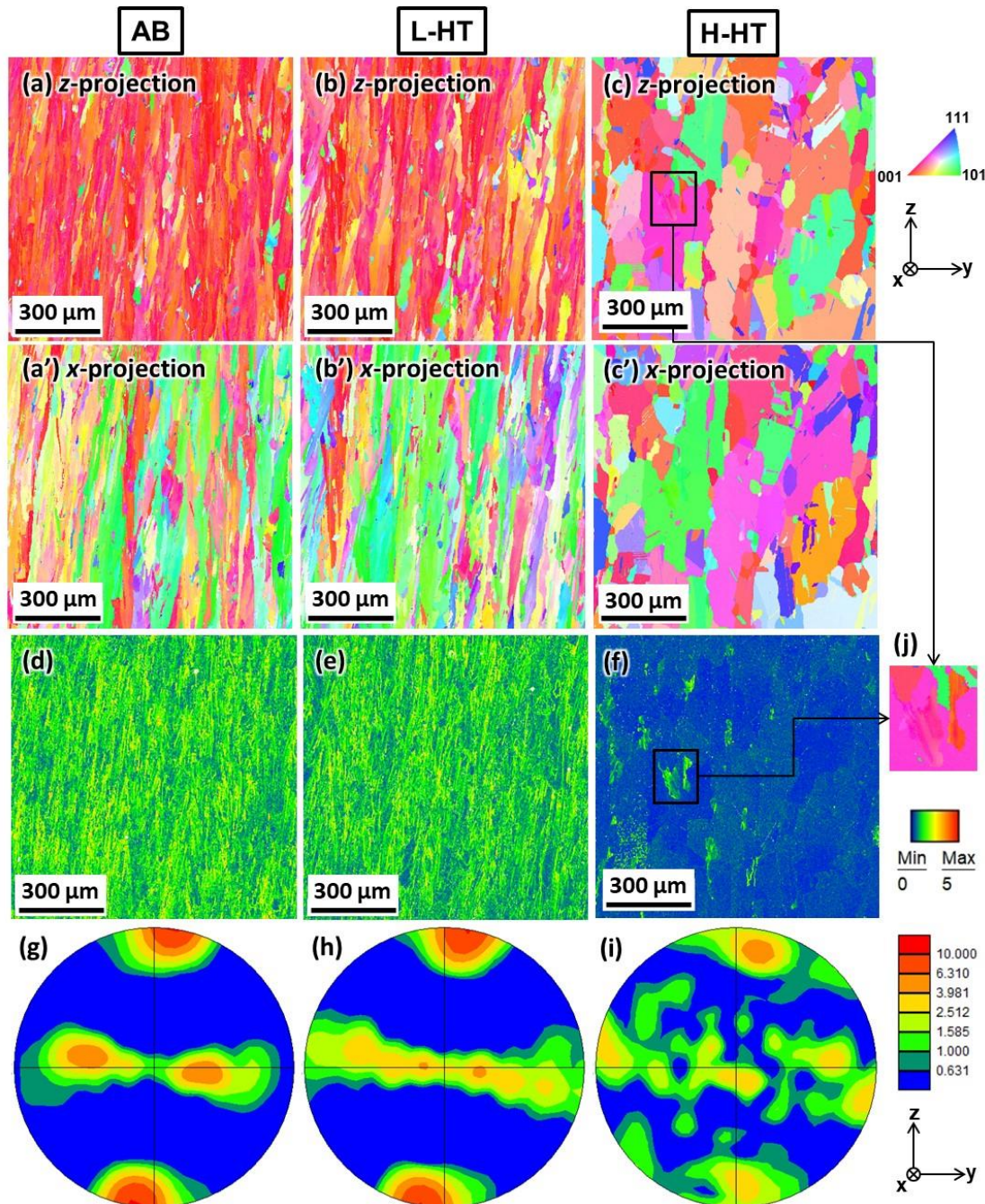


**Figure 3.** (a–c,j) IPF maps, (d–f) KAM maps, and (g–i)  $\{001\}$  pole figures for (a,d,g) AB, (b,e,h) L-HT-ed, and (c,f,i,j) H-HT-ed materials, obtained from the  $y$ - $z$  plane. The IPF maps are projected (a–c,j) from the  $z$ -direction and (a'–c') from the  $x$ -direction.

Figure 4 displays images obtained by backscattered electrons SEM (BSE-SEM). Microcracks, which are well known in the LPBF process of  $\gamma'$  precipitation strengthening alloys [40], were not observed in all of the AB, L-HT-ed, and H-HT-ed materials. The AB material (Figure 4a) had a submicron width cell-solidified microstructure along the

z-direction, and no precipitation of  $\gamma'$  phase was observed. Since the image contrast (chemical or misorientation) of the same submicron width was also observed in Figure 4b,b', it can be confirmed that the cell-solidified microstructure has not been changed after L-HT. The  $\gamma'$  phase after L-HT was inhomogeneous in size and coarser than H-HT-ed materials. In the recrystallized H-HT-ed material, the cell-solidified microstructure disappeared, and the  $\gamma'$  phase was fine and uniform (Figure 4c'). The EDX measurement on the white precipitates, indicated by an arrow in Figure 4c', revealed the segregation of the MC carbide-forming elements, Ta, Nb, and Ti, in IN738LC [34]. On the other hand, the segregation of Mo, the  $M_6C$  carbide-forming element, was not observed. Therefore, the white precipitates were identified as the MC carbides. Messe et al. [36] reported no formation of  $M_6C$  carbides in the as-built condition and after heat treatment of LPBF-processed IN738LC, which is consistent with the results. The MC carbides were aligned in the z-direction and were distributed inside the recrystallized grains. The smaller white precipitates were observed only at the cell boundaries in the AB material and at both the cell boundaries and the grain boundaries in the L-HT-ed material. Here, the region with the same cell growth direction was regarded as a single grain.

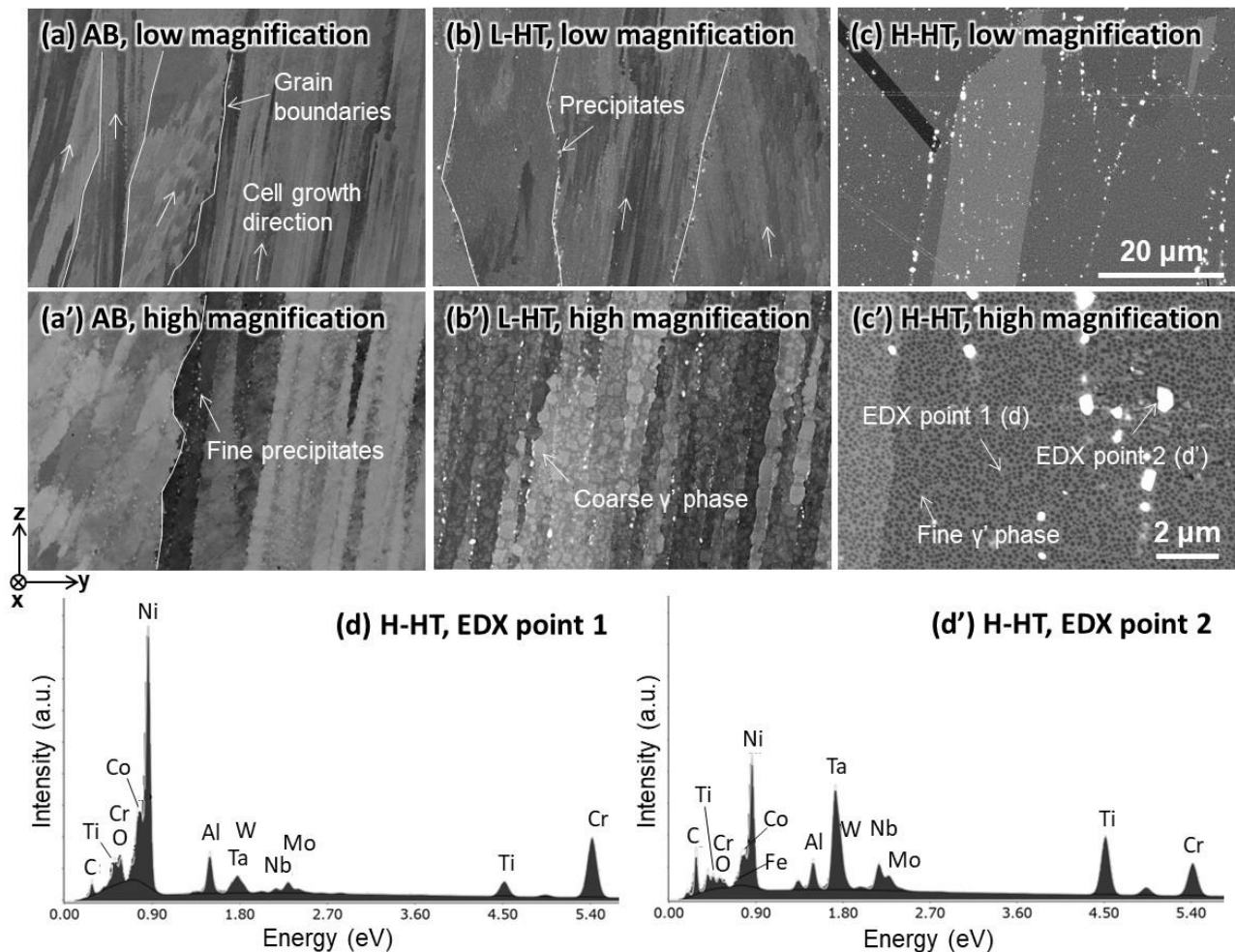


**Figure 4.** SEM images of (a,a') AB, (b,b') L-HT-ed, and (c,c') H-HT-ed materials with two magnifications. EDX spectra obtained from H-HT-ed material at (d) point 1 and (d') point 2.

### 3.2. Tensile Properties Depending on Test Direction and Heat Treatment Conditions

The tensile properties depending on the heat treatment conditions, tensile direction, and test temperature are shown in Figure 5. The average and standard deviations of 0.2% proof stress, tensile strength, and elongation at break are summarized. Table 3 summarizes

the Taylor factor and average grain size obtained from EBSD measurements. The angle of the major axis was calculated using the  $-y$ -direction as  $0^\circ$  and the  $+z$ -direction as  $90^\circ$ . Since the ellipse angles of the AB-, L-HT-ed, and H-HT-ed materials were similar (approximately  $96^\circ$ ), the major and minor axes lengths were regarded as the average grain sizes in the  $z$ - and  $x$ -direction, respectively.

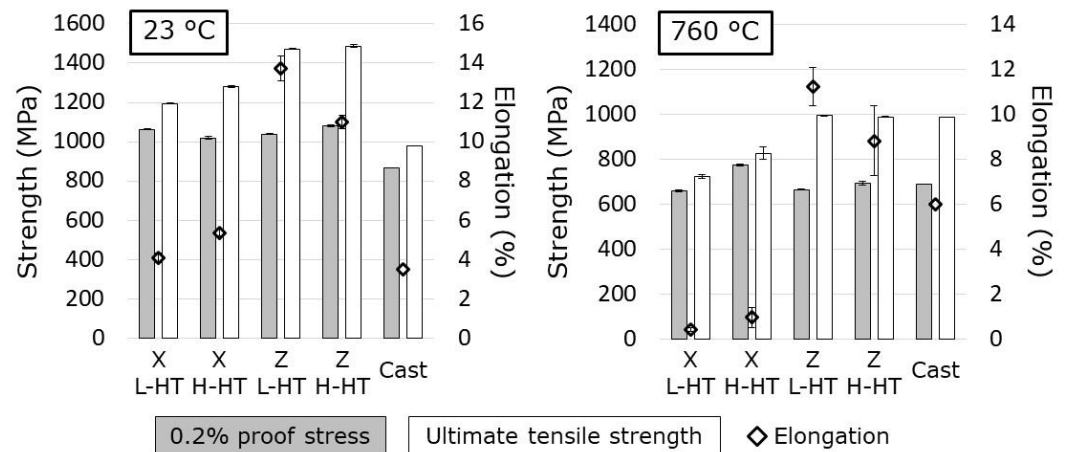


**Figure 5.** Summary of tensile properties. Heat treatment conditions, tensile direction, and test temperature were varied. The typical values of IN738LC castings [39] are also shown.

**Table 3.** Taylor factor and average grain size before and after heat treatments.

Condition	Taylor Factor		Average Grain Size [ $\mu\text{m}$ ] (Ellipse Fit)			Ellipse Angle ( $+z//90^\circ$ )
	$x$ -Direction	$z$ -Direction	Minor Axis ( $x$ -Direction)	Major Axis ( $z$ -Direction)	Aspect Ratio (Minor Axis/Major Axis)	
AB	3.07	2.55	17.2	193.7	0.089	$96.6^\circ$
L-HT	2.91	2.55	19.3	212.5	0.091	$96.9^\circ$
H-HT	3.01	2.83	40.3	141.8	0.284	$95.9^\circ$

First, we focused on the tensile properties at a room temperature of  $23^\circ\text{C}$ . The tensile properties of the LPBF-processed samples exceeded those of the IN738LC castings owing to the Hall–Petch relationship regardless of the tensile direction and heat treatment conditions. In the  $Z$ -samples, the 0.2% proof stress of the H-HT-ed materials was higher than that of the L-HT-ed materials. This is consistent from three viewpoints: finer average grain size (L-LT:  $212.5\ \mu\text{m}$ , H-HT:  $141.8\ \mu\text{m}$ ), higher Taylor factor after recrystallization (L-LT: 2.55, H-HT: 2.83), and finer  $\gamma'$  phase precipitation [41] of the H-HT-ed materials. Corresponding to the increase in 0.2% proof stress, the H-HT-ed materials exhibited high tensile strength and slightly decreased ductility. In contrast to the  $Z$ -samples, the 0.2% proof stress of the  $X$ -samples was higher for the L-HT-ed materials than for the H-HT-ed materials. The almost similar Taylor factor (L-LT: 2.91, H-HT: 3.01) could not explain the difference; then, it was considered that the effect of improving the 0.2% proof stress of the smaller average grain size (L-HT:  $19.3\ \mu\text{m}$ , H-HT:  $40.3\ \mu\text{m}$ ) in the L-HTed materials was stronger than that of the finer  $\gamma'$  phase precipitation in the H-HT-ed materials. The  $Z$ -samples were superior to the  $X$ -samples in terms of both strength and ductility. Stress in the  $x$ -direction promotes crack propagation through mode I opening in columnar grains [42], which is considered to cause an early fracture. This phenomenon was observed in the comparison of the L-HT-ed and H-HT-ed materials in the  $X$ -samples; that is, the recrystallized microstructure (aspect ratio 0.284) in the H-HT-ed materials exhibited better tensile strength and elongation at break than the fine columnar microstructure (aspect ratio 0.091) in the L-HT-ed materials.

Subsequently, the tensile properties at  $760^\circ\text{C}$  were investigated. The tensile properties of the  $Z$ -samples were nearly the same as those of the IN738LC castings. This is because the

Hall–Petch relationship was lost at higher temperatures [43], and the contribution of the  $\gamma'$  phase to inhibiting dislocation migration increased [44]. In the Z-sample, the H-HT-ed materials exhibited a slightly higher 0.2% proof stress and lower ductility than the L-HT-ed materials, similar to the relationship at room temperature. In the X-samples, the decrease in tensile strength and elongation was significant, and it was considerably lower than that of the IN738LC castings. In particular, the elongation at break was as small as approximately 1%, indicating that the fracture occurred immediately after the start of plastic deformation. In addition, fracture without work hardening also resulted in lower tensile strength.

### 3.3. Identification of Fracture Location in X-Samples

The fracture surfaces of the X-samples subjected to tensile tests at 760 °C are shown in Figure 6. The L-HT-ed and H-HT-ed materials were observed at various magnifications, and EDX measurements were performed on distinct particles inside the dimples observed in the H-HT-ed material.

At low magnification (Figure 6a,b), concavo-convex shapes were observed on the entire fracture surface of both the L-HT-ed and H-HT-ed materials. The origin of the fracture has not been clearly identified. Observations at medium magnification (Figure 6a',b') clarified that the concavo-convex shapes roughly corresponded to the shape and size of the grains. In particular, for the L-HT-ed material, columnar grains along the z-direction appeared on the fracture surface, and no dimples were observed. Therefore, it was found that the brittle fracture at the grain boundaries resulted in a very low elongation at a break of 0.4% on average in the L-HT-ed materials.

In contrast, the H-HT-ed material had larger concavo-convex shapes than the L-HT-ed material, suggesting the fracture at the grain boundaries of the coarse recrystallized grains. The area indicated by white arrows in the medium-magnification image (Figure 6b') was similar to the fracture morphology observed in the L-HT-ed material, indicating that non-recrystallized grains, even after H-HT, displayed in Figure 3j, were involved in the fracture. As shown in the high-magnification image, the dimpled area (Figure 6b'') and planar area (Figure 6b''') co-existed. MC carbides, mainly composed of (Ta, Nb, Ti) C, were present inside the dimples, as identified by the EDX spectra (Figure 6d). The appearance of such particles inside the dimples is well known in the fracture of LPBF-processed materials, including inclusions [45]. Therefore, it was considered that the MC carbide (Figure 4c) distributed inside the recrystallized grains was exposed because of the fracture. Consequently, it was clarified that ductile fracture also partially occurred in the recrystallized grains, resulting in an average elongation of 1.0%.

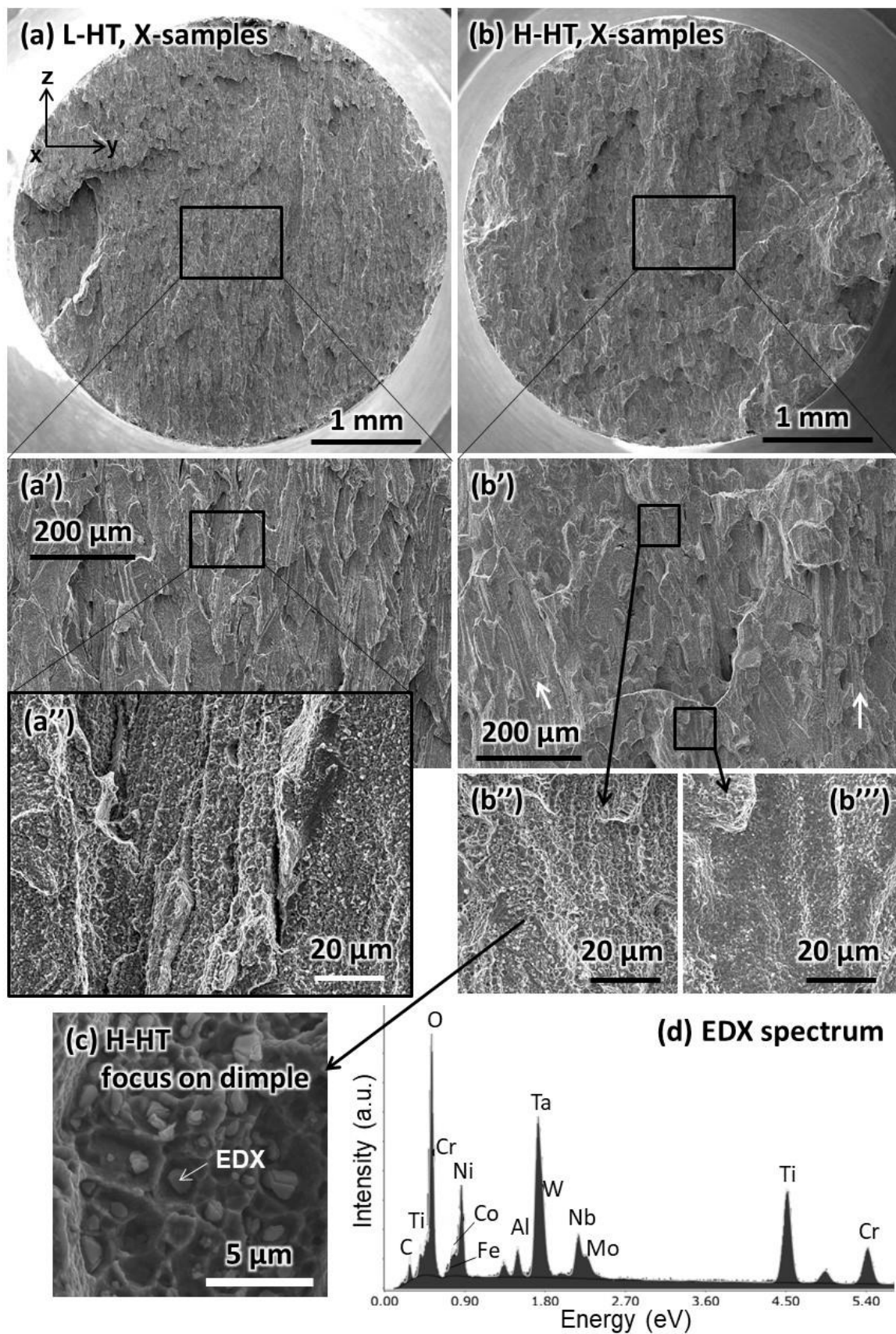


**Figure 6.** Fracture surface of (a–a'') L-HT-ed and (b–b''',c) H-HT-ed materials with various magnifications. (d) EDX spectrum measured at the point indicated in (c).

## 4. Discussion

### 4.1. Microstructure Evolution during Heat Treatment

We discuss the evolution of the microstructure under the two heat treatment conditions. Figure 7 schematically illustrates how the crystal orientation, grain shape, grain size, and MC carbide distributions are determined.

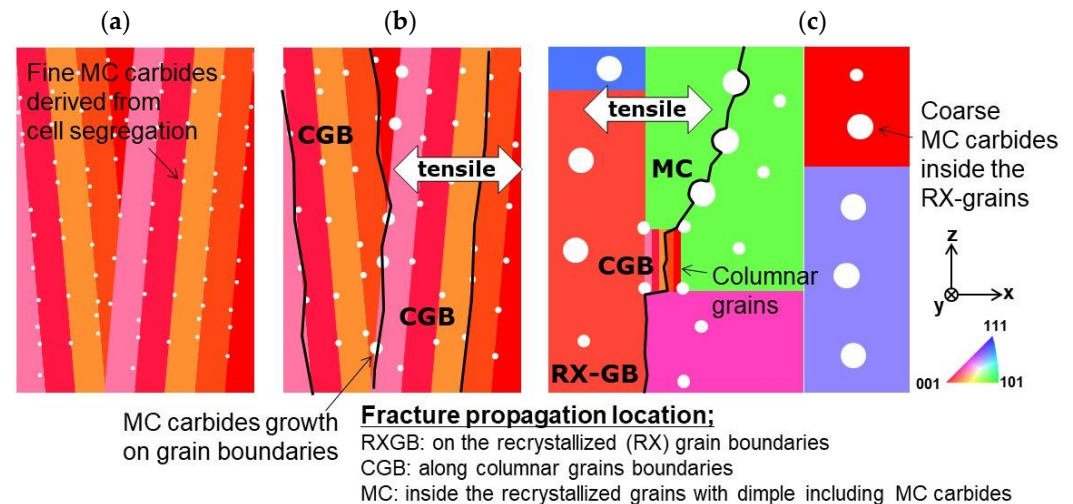


**Figure 7.** Schematics of microstructure evolution during heat treatment. (a) As-built; (b) Heat-treated under the recrystallized Temperature (L-HT); (c) After recrystallization (H-HT).

In the as-built state, the cell-solidified microstructure along the  $z$ -direction via the LPBF process is shown in Figure 7a. Since Nb and Ta, which are MC carbide-forming elements, segregate on the cell boundaries and dendrite boundaries [46,47], the fine white particles at the cell boundaries in the AB materials observed in the BSE image of Figure 3a' are suggested to be fine MC carbides. These fine MC carbides frequently precipitated throughout the cell boundaries.

Next, as shown in Figure 7b, the cell-solidified microstructure and crystal orientation did not change even after heat treatment below the recrystallization temperature (i.e., L-HT). This is confirmed by the fact that the IPF maps and grain sizes (both major axis length and minor axis length) of the AB- and L-HT-ed materials are almost the same. However, the MC carbides, which were finely precipitated in the AB material, aggregated and grew during the heat treatment while being aligned in the  $z$ -direction. This evolution of the MC carbides is supported by the presence of both fine MC carbides at the cell boundaries (Figure 3b') and slightly coarse MC carbides at the grain boundaries (Figure 3b) in the SEM images of the L-HT-ed materials. This is presumably because misorientation between the different cell growth directions results in higher interfacial energies, and, thus, the driving force for MC carbide growth is stronger at the grain boundaries than at the cell boundaries.

Finally, heat treatment at higher temperatures caused the homogenization of segregation and recrystallization (Figure 7c). The randomization of the crystal orientation, grain coarsening, shape change of grains, disappearance of fine MC carbides remaining at the cell boundaries, and growth of coarser MC carbides within the recrystallized grains occur. The coarser MC carbides are arranged in the  $z$ -direction at intervals of approximately 10–30  $\mu\text{m}$ , which is consistent with the distribution of the MC carbides at the old grain boundaries in the L-HT-ed materials. Therefore, it can be deduced that the distribution of the coarser MC carbides inside the recrystallized grains is derived from the grain boundaries originally formed during the LPBF process. As previously shown in Table 3, the recrystallized grains are not fine columnar in shape but slightly elongated in the  $z$ -direction with an aspect ratio of 0.284 (minor axis length/major axis length). This indicates that the grain growth in the  $x$ -direction may have been inhibited by these MC carbides.

In the discussion, the importance of controlling the cell growth directions and the grain boundary distribution within the as-built materials is drawn to obtain the desired recrystallized microstructure, including grain shape, grain size, and MC carbide distribution.

#### 4.2. Future Prospects for Improvement of High-Temperature Strength

We examined how the recrystallization of LPBF-processed IN738LC affects its mechanical properties and anisotropy. To the best of our knowledge, this is the first report on the effect of recrystallization, especially on the anisotropic tensile properties at both room and high temperatures. Thus, the issue of inferior tensile properties in the  $x$ -direction at high temperatures becomes particularly clear. The fracture location is shown schematically in Figure 7, which corresponds to the microstructural evolution during the heat treatment.

The L-HT-ed materials, which did not recrystallize, exhibited fractures where columnar grains were separated, as shown in Figure 7b. The crystallographic texture unique to the LPBF process was achieved by intentionally controlling the cell growth direction [6,19], and the texture exhibited distinct mechanical properties [23]. However, as the cell growth direction coincided, the high-temperature strength in the unintended load direction deteriorated. Therefore, if LPBF-processed materials in a nonrecrystallized state are adopted in the industry, it is necessary to understand the requirements, such as service temperature, load direction, and stress amplitude.

In contrast, recrystallized H-HT-ed materials are easier to handle than L-HT-ed materials. As shown in Figure 7c, the following three aspects can be considered for an improvement in tensile strength and ductility: (1) nonrecrystallized region, (2) recrystallized grain boundaries, and (3) fracture involving MC carbides.

- (1) It is clear that the nonrecrystallized region is undesirable, considering the results for the L-HT-ed materials. In general, the progress of recrystallization can be controlled by both temperature and holding time [48]. Therefore, by optimizing the heat treatment conditions, the nonrecrystallized region (as shown in Figure 3j) can be eliminated.
- (2) Fractures at the recrystallized grain boundaries may cause ductility degradation; thus, the addition of grain boundary strengthening elements, including B and Zr, among others, can be effective. In particular, the IN738LC powder used in this study had a B-value of 0.004 wt.%, much smaller than that of general IN738LC castings (0.010 wt.%) [34]. To optimize the value of B, it is necessary to consider the promotion of microcracks in the LPBF process owing to the segregation of B [49].
- (3) The MC carbides appeared in almost all the dimples, suggesting that they acted as “inclusions” to inhibit dislocation migration, although these dimples may have contributed to the slight ductility. Here, the word “inclusion(s)” is used because the size of the MC carbide was determined to be several hundred nanometers too large against the Burgers vector and, hence, would not lead to increased strength. In general, oxide dispersion-strengthened alloys have very fine oxide particles, 5–50 nm in size [50]. The amount of MC carbides can be controlled by the content of MC carbide former elements, such as Ta, Nb, and Ti [34]. In addition, there is a research example of an AM process in which metal powder is mixed with TiC particles for strengthening by MC carbides [51]. Therefore, by optimizing the heat treatment conditions, segregation at the cell grain boundaries, or the content of MC carbide former elements, the fine MC carbides are positively dispersed inside the recrystallized grains, which may lead to control of the mechanical properties.

When these optimizations improve the ductility in the  $x$ -direction, the plastic deformation behavior and its anisotropy will be an interesting challenge to be investigated.

## 5. Conclusions

In this study, we examined the effects of recrystallization on the tensile properties and anisotropy of the LPBF-processed  $\gamma'$  precipitation-strengthened alloy IN738LC. The following conclusions were drawn:

- (1) A columnar grain microstructure with the first orientation in the  $[001]//z$ -direction and the second orientation rotated randomly in the  $x$ - $y$  plane was obtained by the rotation scan strategy. It did not recrystallize after ST at 1120 °C but recrystallized by HIP and ST at 1204 °C.
- (2) The tensile properties strongly depend on whether recrystallization occurred as well as on the tensile direction. This can be explained by microstructure characterization, featuring the Taylor factor in the tensile direction, average grain size estimated by ellipse approximation, and the relationship between the grain shape and tensile direction.
- (3) The shape of the recrystallized grains and the distribution of coarse MC carbides inside the recrystallized grains were determined by the microstructure in the as-built state. This suggests the importance of controlling the cell solidification direction and grain boundary distribution before recrystallization.
- (4) In the high-temperature tensile tests in the  $x$ -direction, a brittle fracture caused by the separation of the columnar grains occurred. In contrast, dimples were observed at the fracture surface after recrystallization, indicating the possibility of further improvement in ductility.

This is the first report elucidating the effect of recrystallization on the anisotropic tensile properties in the tensile direction at both room and high temperatures and how the mechanical properties of LPBF-processed  $\gamma'$  precipitation-strengthened alloys are explained by microstructural characterization. To improve high-temperature tensile properties in the  $x$ -direction, further study on the promotion of full recrystallization, optimization of grain boundary strengthening, and MC carbide distribution control is required before widespread industrial utilization.

**Author Contributions:** Conceptualization, S.H., M.A. and T.N.; methodology, S.H., K.F. and T.I.; validation, S.H. and K.F.; investigation, S.H., K.F. and T.I.; data curation, S.H. and K.F.; writing—original draft preparation, S.H.; writing—review and editing, T.I. and T.N.; visualization, S.H. and K.F.; supervision, M.A., T.I. and T.N.; project administration, M.A. and T.N. All authors have read and agreed to the published version of the manuscript.

**Funding:** This work was supported by the Cross-Ministerial Strategic Innovation Promotion Program (SIP), Materials Integration for Revolutionary Design System of Structural Materials, Domain C1: “Development of Additive Manufacturing Process for Ni-Based Alloy” from the Japan Science and Technology Agency (JST).

**Institutional Review Board Statement:** Not applicable.

**Informed Consent Statement:** Not applicable.

**Data Availability Statement:** The data supporting the findings of this study are available from the corresponding author upon reasonable request.

**Conflicts of Interest:** The authors declare no conflict of interest.

## References

1. Zhu, J.H.; Zhang, W.H.; Xia, L. Topology optimization in aircraft and aerospace structures design. *Arch. Comput. Methods Eng.* **2016**, *23*, 595–622. [[CrossRef](#)]
2. Plocher, J.; Panesar, A. Review on design and structural optimisation in additive manufacturing: Towards next-generation lightweight structures. *Mater. Des.* **2019**, *183*, 108164. [[CrossRef](#)]
3. Ikeo, N.; Fukuda, H.; Matsugaki, A.; Inoue, T.; Serizawa, A.; Matsuzaka, T.; Ishimoto, T.; Ozasa, R.; Gokcekaya, O.; Nakano, T. 3D puzzle in cube pattern for anisotropic/isotropic mechanical control of structure fabricated by metal additive manufacturing. *Crystals* **2021**, *11*, 959. [[CrossRef](#)]

4. Mower, T.M.; Long, M.J. Mechanical behavior of additive manufactured, powder-bed laser-fused materials. *Mater. Sci. Eng. A* **2016**, *651*, 198–213. [[CrossRef](#)]
5. Tsutsumi, Y.; Ishimoto, T.; Oishi, T.; Manaka, T.; Chen, P.; Ashida, M.; Doi, K.; Katayama, H.; Hanawa, T.; Nakano, T. Crystallographic texture- and grain boundary density-independent improvement of corrosion resistance in austenitic 316L stainless steel fabricated via laser powder bed fusion. *Addit. Manuf.* **2021**, *45*, 102066. [[CrossRef](#)]
6. Ishimoto, T.; Wu, S.Q.; Ito, Y.; Sun, S.H.; Amano, H.; Nakano, T. Crystallographic orientation control of 316L austenitic stainless steel via selective laser melting. *ISIJ Int.* **2020**, *60*, 1758–1764. [[CrossRef](#)]
7. Liu, M.; Wada, T.; Suzuki, A.; Takata, N.; Kobashi, M.; Kato, M. Effect of annealing on anisotropic tensile properties of Al-12%Si alloy fabricated by laser powder bed fusion. *Crystals* **2020**, *10*, 1007. [[CrossRef](#)]
8. Takase, A.; Ishimoto, T.; Suganuma, R.; Nakano, T. Lattice distortion in selective laser melting (SLM)-manufactured unstable,  $\beta$ -type Ti-15Mo-5Zr-3Al alloy analyzed by high-precision X-ray diffractometry. *Scr. Mater.* **2021**, *201*, 113953. [[CrossRef](#)]
9. Takase, A.; Ishimoto, T.; Morita, N.; Ikee, N.; Nakano, T. Comparison of phase characteristics and residual stresses in Ti-6Al-4V alloy manufactured by laser powder bed fusion (L-PBF) and electron beam powder bed fusion (EB-PBF) techniques. *Crystals* **2021**, *11*, 796. [[CrossRef](#)]
10. Ishimoto, T.; Ozasa, R.; Nakano, K.; Weinmann, M.; Schnitter, C.; Stenzel, M.; Matsugaki, A.; Nagase, T.; Matsuzaka, T.; Todai, M.; et al. Development of TiNbTaZrMo bio-high entropy alloy (BioHEA) super-solid solution by selective laser melting, and its improved mechanical property and biocompatibility. *Scr. Mater.* **2021**, *194*, 113658. [[CrossRef](#)]
11. Ikeda, T.; Yonehara, M.; Ikeshoji, T.T.; Nobuki, T.; Hatate, M.; Kuwabara, K.; Otsubo, Y.; Kyogoku, H. Influences of process parameters on the microstructure and mechanical properties of CoCrFeNiTi based high-entropy alloy in a laser powder bed fusion process. *Crystals* **2021**, *11*, 549. [[CrossRef](#)]
12. Hagihara, K.; Ishimoto, T.; Suzuki, M.; Ozasa, R.; Matsugaki, A.; Wang, P.; Nakano, T. Factor which governs the feature of texture developed during additive manufacturing; clarified from the study on hexagonal C40-NbSi<sub>2</sub>. *Scr. Mater.* **2021**, *203*, 114111. [[CrossRef](#)]
13. Walachowicz, F.; Bernsdorf, I.; Papenfuss, U.; Zeller, C.; Graichen, A.; Navrotsky, V.; Rajvanshi, N.; Kiener, C. Comparative energy, resource and recycling lifecycle analysis of the industrial repair process of gas turbine burners using conventional machining and additive manufacturing. *J. Ind. Ecol.* **2017**, *21*, S203–S215. [[CrossRef](#)]
14. Nomura, Y.; Igashira, K. Research and development on customized anisotropic components for aerospace and energy systems. *Mater. Jpn.* **2015**, *54*, 511–512. [[CrossRef](#)]
15. Min, Z.; Huang, G.; Parbat, S.N.; Yang, L.; Chyu, M.K. Experimental investigation on additively manufactured transpiration and film cooling structures. *J. Turbomach.* **2019**, *141*, 031009. [[CrossRef](#)]
16. Caiazzo, F.; Alfieri, V.; Corrado, G.; Argenio, P. Laser powder-bed fusion of Inconel 718 to manufacture turbine blades. *Int. J. Adv. Manuf. Technol.* **2017**, *93*, 4023–4031. [[CrossRef](#)]
17. Hibino, S. Development of manufacturing technology for Ni-base superalloys powder. *Mater. Jpn.* **2021**, *60*, 634–638. [[CrossRef](#)]
18. Nie, P.L.; Ojo, O.A.; Li, Z.G. Numerical modeling of microstructure evolution during laser additive manufacturing of a nickel-based superalloy. *Acta Mater.* **2014**, *77*, 85–95. [[CrossRef](#)]
19. Ishimoto, T.; Hagihara, K.; Hisamoto, K.; Sun, S.H.; Nakano, T. Crystallographic texture control of beta-type Ti-15Mo-5Zr-3Al alloy by selective laser melting for the development of novel implants with a biocompatible low Young's modulus. *Scr. Mater.* **2017**, *132*, 34–38. [[CrossRef](#)]
20. Kok, Y.; Tan, X.P.; Wang, P.; Nai, M.L.S.; Loh, N.H.; Liu, E.; Tor, S.B. Anisotropy and heterogeneity of microstructure and mechanical properties in metal additive manufacturing: A critical review. *Mater. Des.* **2018**, *139*, 565–586. [[CrossRef](#)]
21. Sun, S.H.; Hagihara, K.; Nakano, T. Effect of scanning strategy on texture formation in Ni-25 at.% Mo alloys fabricated by selective laser melting. *Mater. Des.* **2018**, *140*, 307–316. [[CrossRef](#)]
22. Sun, S.H.; Ishimoto, T.; Hagihara, K.; Tsutsumi, Y.; Hanawa, T.; Nakano, T. Excellent mechanical and corrosion properties of austenitic stainless steel with a unique crystallographic lamellar microstructure via selective laser melting. *Scr. Mater.* **2019**, *159*, 89–93. [[CrossRef](#)]
23. Gokcekaya, O.; Ishimoto, T.; Hibino, S.; Yasutomi, J.; Narushima, T.; Nakano, T. Unique crystallographic texture formation in Inconel 718 by laser powder bed fusion and its effect on mechanical anisotropy. *Acta Mater.* **2021**, *212*, 116876. [[CrossRef](#)]
24. Hagihara, K.; Nakano, T. Control of anisotropic crystallographic texture in powder bed fusion additive manufacturing of metals and ceramics-A review. *JOM* **2022**, *74*, 1760–1773. [[CrossRef](#)]
25. Gokcekaya, O.; Hayashi, N.; Ishimoto, T.; Ueda, K.; Narushima, T.; Nakano, T. Crystallographic orientation control of pure chromium via laser powder bed fusion and improved high temperature oxidation resistance. *Addit. Manuf.* **2020**, *36*, 101624. [[CrossRef](#)]
26. Hibino, S.; Todo, T.; Ishimoto, T.; Gokcekaya, O.; Koizumi, Y.; Igashira, K.; Nakano, T. Control of crystallographic texture and mechanical properties of Hastelloy-X via laser powder bed fusion. *Crystals* **2021**, *11*, 1064. [[CrossRef](#)]
27. Weavwe, J.S.; Rosenthal, I. *Understanding Anisotropic Tensile Properties of Laser Powder Bed Fusion Additive Metals: A Detailed Review of Select Examples*; Advanced Manufacturing Series (NIST AMS) 100-44; National Institute of Standards and Technology: Gaithersburg, MD, USA, 2021. [[CrossRef](#)]

28. Tomus, D.; Tian, Y.; Rometsch, P.A.; Heilmaier, M.; Wu, X.H. Influence of post heat treatments on anisotropy of mechanical behaviour and microstructure of Hastelloy-X parts produced by selective laser melting. *Mater. Sci. Eng. A* **2016**, *667*, 42–53. [[CrossRef](#)]
29. Hosseini, E.; Popovich, V.A. A review of mechanical properties of additively manufactured Inconel 718. *Addit. Manuf.* **2019**, *30*, 100877. [[CrossRef](#)]
30. Kanagarajah, P.; Brenne, F.; Niendorf, T.; Maier, H.J. Inconel 939 processed by selective laser melting: Effect of microstructure and temperature on the mechanical properties under static and cyclic loading. *Mater. Sci. Eng. A* **2013**, *588*, 188–195. [[CrossRef](#)]
31. Geiger, F.; Kunze, K.; Etter, T. Tailoring the texture of IN738LC processed by selective laser melting (SLM) by specific scanning strategies. *Mater. Sci. Eng. A* **2016**, *661*, 240–246. [[CrossRef](#)]
32. Zhao, J.R.; Hung, F.Y.; Lu, C.S.; Lai, I.C. Comparison of laser powder bed fusion and cast Inconel 713 alloy in terms of their microstructure, mechanical properties, and fatigue life. *Adv. Eng. Mater.* **2021**, *23*, 2001366. [[CrossRef](#)]
33. Munoz-Moreno, R.; Divya, V.D.; Driver, S.L.; Messe, O.; Illston, T.; Baker, S.; Carpenter, M.A.; Stone, H.J. Effect of heat treatment on the microstructure, texture and elastic anisotropy of the nickel-based superalloy CM247LC processed by selective laser melting. *Mater. Sci. Eng. A* **2016**, *674*, 529–539. [[CrossRef](#)]
34. Sims, C.T.; Stoloff, N.S.; Hagel, W.C. *Superalloys II: High-Temperature Materials for Aerospace and Industrial Power*; John Wiley & Sons: Hoboken, NJ, USA, 1987; pp. 97–133.
35. Kunze, K.; Etter, T.; Grasslin, J.; Shklover, V. Texture, anisotropy in microstructure and mechanical properties of IN738LC alloy processed by selective laser melting (SLM). *Mater. Sci. Eng. A* **2015**, *620*, 213–222. [[CrossRef](#)]
36. Messe, O.; Munoz-Moreno, R.; Illston, T.; Baker, S.; Stone, H.J. Metastable carbides and their impact on recrystallisation in IN738LC processed by selective laser melting. *Addit. Manuf.* **2018**, *22*, 394–404. [[CrossRef](#)]
37. Gu, D.D.; Shen, Y.F. Effects of processing parameters on consolidation and microstructure of W-Cu components by DMLS. *J. Alloys Compd.* **2009**, *473*, 107–115. [[CrossRef](#)]
38. Keshavarzkermani, A.; Esmaeilzadeh, R.; Ali, U.; Enrique, P.D.; Mahmoodkhani, Y.; Zhou, N.Y.; Bonakdar, A.; Toyserkani, E. Controlling mechanical properties of additively manufactured hastelloy X by altering solidification pattern during laser powder-bed fusion. *Mater. Sci. Eng. A* **2019**, *762*, 138081. [[CrossRef](#)]
39. Brown, W.F., Jr.; Gibson, C. (Eds.) *Aerospace Structural Metals Handbook*, 35th ed.; Code4217; CINDAS/USAF CRDA Handbooks Operation; Purdue University: West Lafayette, IN, USA, 1999; pp. 1–25.
40. Carter, L.N.; Attallah, M.M.; Reed, R.C. Laser powder bed fabrication of nickel-base superalloys: Influence of parameters; Characterisation, quantification and mitigation of cracking. In Proceedings of the Superalloys 2012, Champion PA, USA, 9–13 September 2012; The Minerals, Metals & Materials Society(TMS): Pittsburgh, PA, USA, 2012; pp. 577–586.
41. Osada, T.; Gu, Y.F.; Nagashima, N.; Yuan, Y.; Yokokawa, T.; Harada, H. Optimum microstructure combination for maximizing tensile strength in a polycrystalline superalloy with a two-phase structure. *Acta Mater.* **2013**, *61*, 1820–1829. [[CrossRef](#)]
42. Ni, M.; Chen, C.; Wang, X.J.; Wang, P.W.; Li, R.D.; Zhang, X.Y.; Zhou, K.C. Anisotropic tensile behavior of in situ precipitation strengthened Inconel 718 fabricated by additive manufacturing. *Mater. Sci. Eng. A* **2017**, *701*, 344–351. [[CrossRef](#)]
43. Schneibel, J.H.; Heilmaier, M. Hall-Petch breakdown at elevated temperatures. *Mater. Trans.* **2014**, *55*, 44–51. [[CrossRef](#)]
44. Kozar, R.W.; Suzuki, A.; Milligan, W.W.; Schirra, J.J.; Savage, M.F.; Pollock, T.M. Strengthening mechanisms in polycrystalline multimodal nickel-base superalloys. *Metall. Mater. Trans. A* **2009**, *40A*, 1588–1603. [[CrossRef](#)]
45. Lou, X.Y.; Andresen, P.L.; Rebak, R.B. Oxide inclusions in laser additive manufactured stainless steel and their effects on impact toughness and stress corrosion cracking behavior. *J. Nucl. Mater.* **2018**, *499*, 182–190. [[CrossRef](#)]
46. Zhang, F.; Levine, L.E.; Allen, A.J.; Campbell, C.E.; Lass, E.A.; Cheruvathur, S.; Stoudt, M.R.; Williams, M.E.; Idell, Y. Homogenization kinetics of a nickel-based superalloy produced by powder bed fusion laser sintering. *Scr. Mater.* **2017**, *131*, 98–102. [[CrossRef](#)] [[PubMed](#)]
47. Tin, S.; Pollock, T.M. Phase instabilities and carbon additions in single-crystal nickel-base superalloys. *Mater. Sci. Eng. A* **2003**, *348*, 111–121. [[CrossRef](#)]
48. Humphries, J.; Rohrer, G.S.; Rollett, A. *Recrystallization and Related Annealing Phenomena*; Elsevier: Amsterdam, The Netherlands, 2017; pp. 245–304.
49. Chauvet, E.; Kontis, P.; Jagle, E.A.; Gault, B.; Raabe, D.; Tassin, C.; Blandin, J.J.; Dendievel, R.; Vayre, B.; Abed, S.; et al. Hot cracking mechanism affecting a non-weldable Ni-based superalloy produced by selective electron beam melting. *Acta Mater.* **2018**, *142*, 82–94. [[CrossRef](#)]
50. Suryanarayana, C.; Al-Aqeeli, N. Mechanically alloyed nanocomposites. *Prog. Mater. Sci.* **2013**, *58*, 383–502. [[CrossRef](#)]
51. Hong, C.; Gu, D.D.; Dai, D.H.; Alkhayat, M.; Urban, W.; Yuan, P.P.; Cao, S.; Gasser, A.; Weisheit, A.; Kelbassa, I.; et al. Laser additive manufacturing of ultrafine TiC particle reinforced Inconel 625 based composite parts: Tailored microstructures and enhanced performance. *Mater. Sci. Eng. A* **2015**, *635*, 118–128. [[CrossRef](#)]